 CMES, vol.74, no.4, pp.247-267, 2011

Numerical Simulation of Gas-assisted Injection Molding Process for A Door Handle

Qiang Li, Jie Ouyang[1], Xuejuan Li[2], Guorong Wu[2] and Binxin Yang[2]

Abstract: A unified mathematical model is proposed to predict the short shot, primary and secondary gas penetration phenomenon in gas-assisted injection molding (GAIM) process, where the Cross-WLF model and two-domain modified Tait equation are employed to simulate the melt viscosity and density in the whole process, respectively. The governing equations of two-phase flows including gas, air and polymer melt are solved using finite volume method with SIMPLEC technology. At first, two kinds of U-shaped gas channels are modeled, where the shape corner and generous corner cases are studied. At last, as a case study, the short shot, primary and secondary gas penetration processes of a door handle are simulated. The numerical results show that the mathematical model can successfully depict the race-tracking and corner effects, which are very helpful for the design of GAIM.

Keywords: Gas-assisted, injection molding, finite volume method, door handle

1 Introduction

Nowadays plastics industry plays a more and more important role in manufacture industries. And about more than 50% molding processes are completed by injection molding, in which gas assisted injection molding (GAIM) is developed a new type of injection molding process [Avery (2001)]. GAIM can reduce the mold cavity pressure-based and avoid forming the structure of rough surfaces generated. Gas-assisted injection technology can be applied to a variety of plastics, such as TV set, computer, bathroom furniture and car door handle etc. Due to plastic product's lower weight, reduce the molding and cooling time, thus GAIM technology will be subject to wider application in the industry. Since the dynamic interaction of gas

[1] Corresponding author. Jie Ouyang, Department of Applied Mathematics, Northwestern Polytechnical University, Xi'an 710129, China. Tel.: +86 29 8849 5234; fax: +86 29 8849 1000. E-mail: jieouyang@nwpu.edu.cn.

[2] Department of Applied Mathematics, Northwestern Polytechnical University, Xi'an 710129, China

and melt is very complex, the numerical simulation of GAIM is more difficult than that of conventional injection molding (CIM).

The gas distribution and gas channel shapes are of great importance to understand and study gas penetration process. In GAIM there are two moving interfaces, gas/melt and melt/air interfaces. Interface tracking is quite necessary for GAIM, and some research works have been done recently. Llubca and Hétu (2002) present a finite element algorithm for solving GAIM problems and two additional transport equations are employed to track the gas/melt and melt/air interfaces. Polynkin et al. (2005) adopt finite element code for the simulation of GAIM, in which two pseudo-concentration functions are used to track two moving interfaces. Zhou et al. (2009) employ the matching asymptotic expansion method to solve the governing equations, while the analytical solution of the gas penetration interface is presented. Li et al. (2011) propose a two-phase flow model to describe the gas and melt flows in GAIM, in which the moving interfaces are traced by level set (LS) method. Chen et al. (2011) apply the Galerkin finite element method discretize the governed equations, and the gas/melt interface is located by the volume of fluid (VOF) method. GAIM in two different L-shaped channel with and without fillet are simulated. The numerical results shows that the edge shape of gas channel greatly affects the gas penetration of GAIM, also the recommended gas channel design is proposed.

All of above literatures only consider primary gas penetration process. After the primary gas penetration finishes, the secondary gas penetration takes place due to further cooling of the polymer melt. The numerical simulations or experimental researches of the secondary gas penetration are studied by [Carrillo and Isayev (2009); Li and ISAYEV (2004); Li et al. (2004); Chau (2008)]. The calculation of the secondary gas penetration is based on the melt shrinkage and compressibility of the polymer melt governed by the P-V-T equation of state originally proposed by Tait [Carrillo and Isayev (2009); Li and ISAYEV (2004); Li et al. (2004)]. The transient gas-liquid interface development and gas penetration behavior during the cavity filling and gas packing stage in GAIM are studied, and the numerical results agree well with those of experiments. Marcilla et al. (2006) propose a mid-plane model of the three-dimensional geometry of the mold cavity to simulate the cavity filling and gas packing steps in the GAIM by the finite element method. Chau (2008) employ the finite volume method for solving the governing equations, and the gas/melt and melt/air interfaces are traced using two front transport equations, in which total gas penetration length is compared with that predicted by other models and experimental data.

In order to study the GAIM process comprehensively, in this paper a unified mathematical model is proposed to predict the short shot, primary and secondary gas penetration phenomenon, where the Cross-WLF model and two-domain modified Tait equation are employed to simulate the melt viscosity and density in the whole process, respectively. The governing equations of two-phase flows are solved using finite volume method with SIMPLEC technology. The CLSVOF method [Mark and Elbridge (2000); Son and Hur (2002); Son (2003); Wang et al. (2008)], which can keeps both the advantages of the LS and VOF (volume-of-fluid) method, is adopt to capture the two moving interfaces in GAIM process. At first, two kinds of U-shaped gas channels with and without shape corner are studied. At last, as a case study, the whole GAIM process of a door handle is simulated.

The content of this paper is listed as follows. First, the mathematical model is proposed in Section 2. The CLSVOF method is introduced in Section 3. Section 4 presents the numerical implementation of the finite volume method and CLSVOF method. In Section 5 the interface tracking capability of the CLSVOF method is tested by two benchmark problems. Then the numerical results of GAIM in two kinds of U-shaped channels is shown and discussed. As a case study, GAIM of a door handle is simulated and analyzed in detail. Some conclusions and future research directions conclude this paper.

2 Mathematical Model

2.1 Governing Equations

In the melt injection phase, both the gas-phase and the liquid-phase can be regarded as incompressible flows [Yang et al. (2010)]. In primary gas penetration process, since the gas velocity is low, both of gas and melt can be treated as the incompressible fluid [Li et al. (2011)]. However, for the secondary gas penetration, the melt compressibility can not be neglected, so both of the gas and melt are treated as compressible flows. In fact, the continuity, momentum and energy equations of the incompressible and compressible fluids can be written as the unified equations in dimensionless form:

$$\frac{\partial \rho}{\partial t}+\frac{\partial (\rho u)}{\partial x}+\frac{\partial (\rho v)}{\partial y}=0, \tag{1}$$

$$\frac{\partial (\rho u)}{\partial t}+\frac{\partial (\rho uu)}{\partial x}+\frac{\partial (\rho vu)}{\partial y}=\frac{\eta}{Re}\left(\frac{\partial^2 u}{\partial x^2}+\frac{\partial^2 u}{\partial y^2}\right)-\frac{\partial p}{\partial x}+\frac{\eta}{3Re}\frac{\partial}{\partial x}\left(\nabla\cdot\mathbf{u}\right), \tag{2}$$

$$\frac{\partial (\rho v)}{\partial t}+\frac{\partial (\rho uv)}{\partial x}+\frac{\partial (\rho vv)}{\partial y}=\frac{\eta}{Re}\left(\frac{\partial^2 v}{\partial x^2}+\frac{\partial^2 v}{\partial y^2}\right)-\frac{\partial p}{\partial y}+\frac{\eta}{3Re}\frac{\partial}{\partial y}\left(\nabla\cdot\mathbf{u}\right), \tag{3}$$

$$Pe\left[\frac{\partial(\rho CT)}{\partial t}+\frac{\partial(\rho CuT)}{\partial x}+\frac{\partial(\rho CvT)}{\partial y}\right]-\left(\frac{\partial^2(\kappa T)}{\partial x^2}+\frac{\partial^2(\kappa T)}{\partial y^2}\right)= Re\cdot Br\left[\frac{\partial p}{\partial t}+\nabla\cdot(p\mathbf{u})-p(\nabla\cdot\mathbf{u})\right]+Br\cdot\eta\cdot I. \quad (4)$$

where $I=2\left(\frac{\partial u}{\partial x}\right)^2+2\left(\frac{\partial v}{\partial y}\right)^2+\left(\frac{\partial u}{\partial y}+\frac{\partial v}{\partial x}\right)^2-\frac{2}{3}(\nabla\cdot\mathbf{u})^2$. $Re=\frac{\rho_m UL}{\eta_m}$ denotes Reynolds number, $Pe=\frac{\rho_m C_m}{\kappa_m}\cdot UL$ Peclet number, $Br=\frac{\eta_m U^2}{\kappa_m T_0}$Brinkman number.

2.2 Interface representation and fluid properties

The gas/melt and melt/air interfaces are represented by the LS function$\phi(\mathbf{x},t)$, which can be defined using the unified form [Li et al. (2011)]. And the sign of $\phi(\mathbf{x},t)$ is that $\phi>0$ in the melt zone and $\phi<0$ in the gas (or air) zones, respectively. Each phase has constant density and viscosity, while the fluid properties near the interface have sharp jumps, which are smoothed over a transition band using the LS function

$$\rho=\rho(\phi)=\rho_{\mathrm{ga}}+(\rho_{\mathrm{m}}-\rho_{\mathrm{ga}})H_\varepsilon(\phi), \quad (5)$$

$$\eta=\eta(\phi)=\eta_{\mathrm{ga}}+(\eta_{\mathrm{m}}-\eta_{\mathrm{ga}})H_\varepsilon(\phi), \quad (6)$$

$$C=C(\phi)=C_g+(C_m-C_{ga})H_\varepsilon(\phi), \quad (7)$$

$$\kappa=\kappa(\phi)=\kappa_{ga}+(\kappa_m-\kappa_{ga})H_\varepsilon(\phi). \quad (8)$$

whereρ, η, C and κ are density, viscosity, thermal capacity and conductivity, respectively. The subscript *ga* and *m* represent gas (or air) and melt respectively. The smoothed Heaviside function is

$$H_\varepsilon(\phi)=\begin{cases}0 & \phi<-\varepsilon\\ \frac{1}{2}\left[1+\frac{\phi}{\varepsilon}+\frac{1}{\pi}\sin\left(\frac{\pi\phi}{\varepsilon}\right)\right] & |\phi|\le\varepsilon\\ 1 & \phi>\varepsilon\end{cases} \quad (9)$$

where ε is a parameter related to the interface thickness, and here $\varepsilon=1.5\Delta x$.

3 CLSVOF method

In the CLSVOF method, the interface is reconstructed via a PLIC (Piecewise Linear Interface Construction) scheme from the VOF function, in which the interface normal vector is computed from the LS function [Mark and Elbridge (2000); Son and Hur (2002); Son (2003); Wang et al. (2008)]. Based on the reconstructed interface, the LS function is reinitialized via the geometric operations to conserve the liquid mass with the aid of the VOF function. The coupling of the LS and VOF methods takes place during the interface reconstruction. The flow chart for the CLSVOF algorithm is shown in Fig. 1.

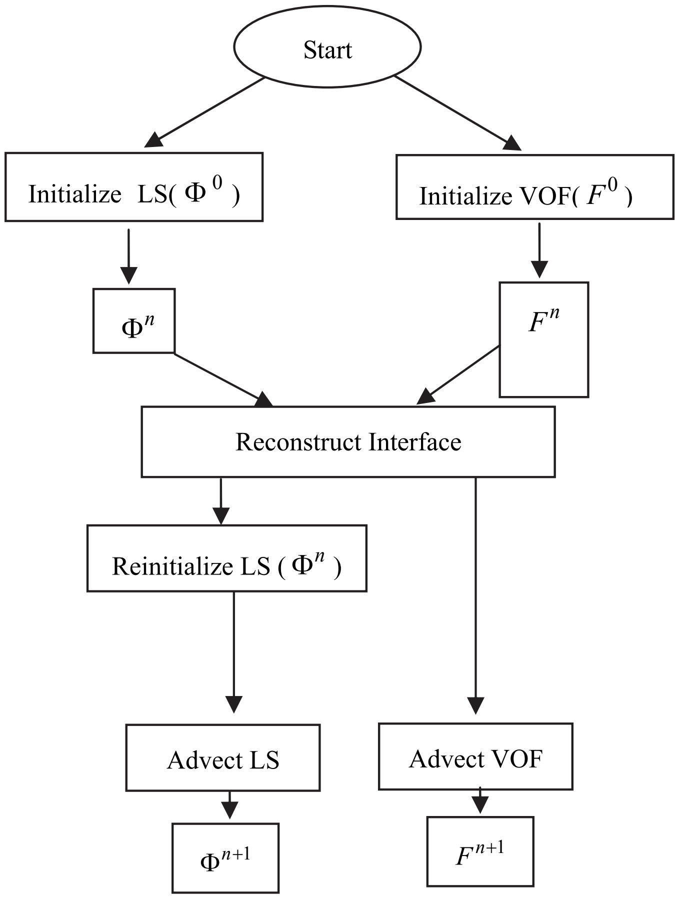

Figure 1: Flow chart of the CLSVOF method.

The LS and VOF functions are advected using the following equations, respectively

$$\frac{D\phi}{Dt} = \frac{\partial \phi}{\partial t} + (\mathbf{u} \cdot \nabla)\,\phi = 0. \tag{10}$$

$$\frac{DF}{Dt} = \frac{\partial F}{\partial t} + (\mathbf{u} \cdot \nabla)\,F = 0, \tag{11}$$

4 Numerical implementation

4.1 Governing equations solver

The governing equations are discretized by the finite volume method on the non-staggered meshes, and all quantities are stored on the same nodes [Li et al. (2011); Yang et al. (2010)]. To solve the problem of the pressure-velocity decoupling, we use SIMPLEC (semi-implicit method for pressure linked equations consistent) method and Momentum Interpolation (MI) on the collocated grids [Li et al. (2011); Yang et al. (2010)]. The continuum Eq. 1 can be expressed as the following formula by integrating in the controlling volume and get,

$$\frac{\left(\rho_P-\rho_P^0\right)\Delta x\Delta y}{\Delta t}+\left[(\rho u)_e-(\rho u)_w\right]\Delta y+\left[(\rho v)_n-(\rho v)_s\right]\Delta x=0. \tag{12}$$

And the discretization of the momentum Eq. 2 can be written as a generalized quantity Φ, that is,

$$a_P\Phi_P=a_E\Phi_E+a_W\Phi_W+a_N\Phi_N+a_S\Phi_S+S_\phi. \tag{13}$$

where S_ϕ is the source term in the momentum equation (see Table 1), and the coefficients a_E,a_W,a_N,a_S,a_P can be expressed as

$$\begin{aligned}
&a_E=D_eA(|P_e|)+\max(-F_e,0),\quad a_W=D_wA(|P_w|)+\max(F_w,0),\\
&a_N=D_nA(|P_n|)+\max(-F_n,0),\quad a_S=D_sA(|P_s|)+\max(F_s,0),\\
&a_P=a_E+a_W+a_N+a_S+a_T+a_B+\delta_1\frac{\Delta x\Delta y}{\Delta t}.
\end{aligned} \tag{14}$$

where P_e, P_s, P_w and P_n are the Peclet numbers on the cell faces; F_e, F_s, F_w and F_n are the cell faces flux; and D_e, D_s, D_w and $D_n$denote diffuse derivatives on the cell faces. The form $A(|P_\Delta|)$can be different according to the method by which the convection terms are discretized. Here a central difference scheme is chosen, i.e. $A(|P_\Delta|)=1-0.5\,|P_\Delta|$. And all the above coefficients are formulated as follows

$$F_e=\delta_1u_{fe}\Delta y\Delta z,\quad D_e=\Gamma\frac{\Delta y\Delta z}{x_E-x_P},\quad P_e=\frac{F_e}{D_e},$$

$$\begin{aligned}
&F_w=\delta_1u_{fw}\Delta y\Delta z,\quad D_w=\Gamma\frac{\Delta y\Delta z}{x_P-x_W},\quad P_w=\frac{F_w}{D_w},\\
&F_n=\delta_2v_{fn}\Delta x\Delta z,\quad D_n=\Gamma\frac{\Delta x\Delta z}{y_N-y_P},\quad P_n=\frac{F_n}{D_n},
\end{aligned} \tag{15}$$

$$F_s = \delta_2 v_{fs} \Delta x \Delta z, \quad D_s = \Gamma \frac{\Delta x \Delta z}{y_P - y_S}, \quad P_s = \frac{F_s}{D_s}.$$

Similarly, the energy Eq. 3 can be discretized in the same way. Then each of the governing equations can be written using the following general conservative form

$$\delta_1 \frac{\partial \Phi}{\partial t} + \frac{\partial}{\partial x}\left(\delta_2 u\Phi - \Gamma \frac{\partial \Phi}{\partial x}\right) + \frac{\partial}{\partial y}\left(\delta_2 v\Phi - \Gamma \frac{\partial \Phi}{\partial y}\right) = S_\phi. \tag{16}$$

For Cartesian coordinates, δ_1, δ_2 and Γ are constants, and Φ and S_ϕ are functions that are defined depending on the particular equation under consideration (see Table 1).

Table 1: Definition of the constants and functions in the general equation (15)

Equation	Φ	δ_1	δ_2	Γ	S_ϕ
Continuity	ρ	1	1	0	0
u-momentum	u	ρ	ρ	$\frac{\eta}{Re}$	$-\frac{\partial p}{\partial x} + \frac{\eta}{3Re}\frac{\partial}{\partial x}(\nabla \cdot \mathbf{u})$
v-momentum	v	ρ	ρ	$\frac{\eta}{Re}$	$-\frac{\partial p}{\partial y} + \frac{\eta}{3Re}\frac{\partial}{\partial y}(\nabla \cdot \mathbf{u})$
energy equation	T	$Pe\rho C_v$	$Pe\rho C_v$	κ	$Re \cdot Br \left[\frac{\partial p}{\partial t} + \nabla \cdot (p\mathbf{u}) - p(\nabla \cdot \mathbf{u})\right] + Br \cdot \eta \cdot I$

4.2 CLSVOF solver

The LS advection function belongs to the Hamilton-Jacobi equations, which is discretized in this paper by the fifth-order WENO (weighted essentially non-oscillatory) scheme in space and third-order TVD (total variation diminishing) Runge-Kutta (R-K) scheme in time, respectively (Yang et al. (2010), Li et al. (2011)).

To solve the VOF function Eq. 10, the flux-splitting algorithm used by Sussman and Puckett [11] is adopted. Son and Hur (2002), Son (2003) have described the VOF advection algorithm very clearly. In these papers s is a parameter related to the shortest distance from the origin (See Son. (2003) for details). Since the normal vector is estimated from the LS function, i.e.$\mathbf{n} = \nabla\phi/|\nabla\phi|$, s is just the shortest distance from the origin. If s and $\mathbf{n}$ are given, F can be calculated immediately, and vice versa (Son and Hur (2002), Son (2003)).

In general, the computational region is usually irregular, to solve this problem the body fitted or unstructured grids could be used, but it is more complex to program. Domain extension method is an alternative technology which can be convenient to implement [Korichi et al. (2009); Nie and Armaly (2002)]. In order to describe the irregular solid region during computation, the dynamic viscosity is set to be a very large value for momentum equation (such as10^{20}), while thermal conductivity is set to be a very small value for energy equation (such as10^{-20}). Thus, the minimum rectangle approximating irregular region is chosen as the computational domain.

5 Results and analysis

5.1 Numerical test for benchmark problems

5.1.1 Zalesak's disk problem

The Zalesak's disk problem [Zalesak (1979)] is usually used to verify the ability of interface capturing methods. A disk with radius 0.15 contains a slotted circle centered at (0.50, 0.75) whose slot width is0.05. The computational domain is 1.00×1.00 with space interval 0.01. The prescribed velocity field is given as follows

$$u = (\pi/3.14)(0.50 - y),$$
$$v = (\pi/3.14)(x - 0.50). \tag{17}$$

with the axis of rotation centered at (0.5,0.5).

The results obtained using LS and CLSVOF methods are compared with the initial shape after a whole rotation. From Fig. 3 it is clear that the sharp edges of the slot are smoothed out in the LS method. The relative mass errors for the CLSVOF and LS methods are about 0.02% and 0.15%, respectively.

5.1.2 Dam break problem

Dam break problem is another good benchmark problem to validate the interface tracking capability of the CLSVOF method for large-density ratio (1000:1) and large-viscosity ratio (10:1) two-phase flow problem. A cube water column with $1h$ units wide is enclosed within a container with $5h$ units long by $1.25h$ units high. The water is initially retained by a dam on the right-hand side of the column. The dam is suddenly removed at time $t = 0$ and the water starts to collapse due to gravity (See Fig. 3). To perform a mesh convergence study, the grid size of the simulation is chosen as60×15,120×30 and 180×45, respectively.

Fig. 4 shows that the numerical results on three different grids are almost the same, and the predicted front positions and height are in an excellent agreement with the experimental data in [Kelecy and Pletcher (1997)].

The Zalesak's disk and dam break problems illustrate that CLSVOF method not only can conserve mass more accurately, but also performs well in two-phase flow problem.

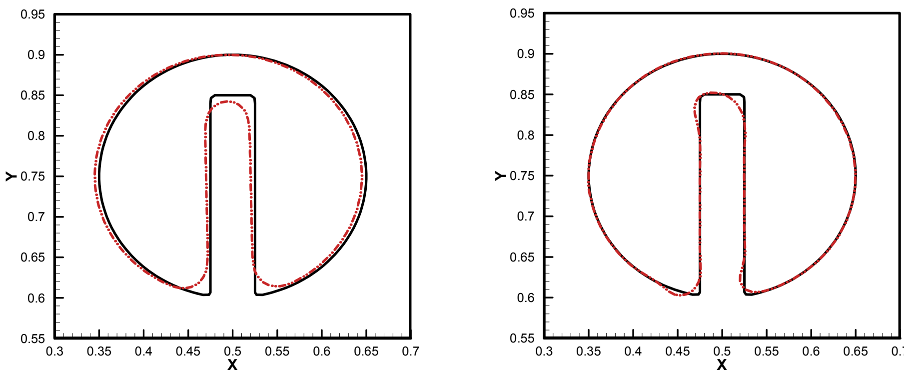

(a) (b)

Figure 2: Zalesak's problem. (a) LS method; (b) CLSVOF method (Solid line: original shape, DashDotDot line: shape after a whole revolution)

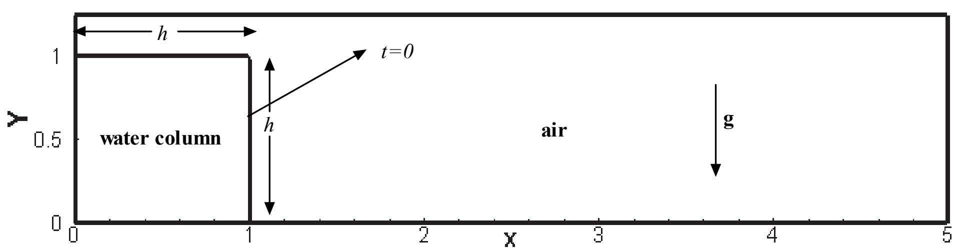

Figure 3: The initial setup of dam break problem.

5.2 *Simulation of GAIM*

In GAIM process, especially in gas-assisted packing phase, the melt viscosity and density change greatly. In order to better describe the melt viscosity, the modified Cross-WLF model is adopted [Li et al. (2011); Chau (2008)]

$$\eta\left(T,\dot{\gamma},p\right)=\frac{\eta_0\left(T,p\right)}{1+\left(\eta_0\dot{\gamma}/\tau^*\right)^{1-n}}, \tag{18}$$

$$\eta_0=\eta_g\exp\left(\frac{-C_1^g\left(T-T_g\right)}{C_2^g+T-T_g}\right). \tag{19}$$

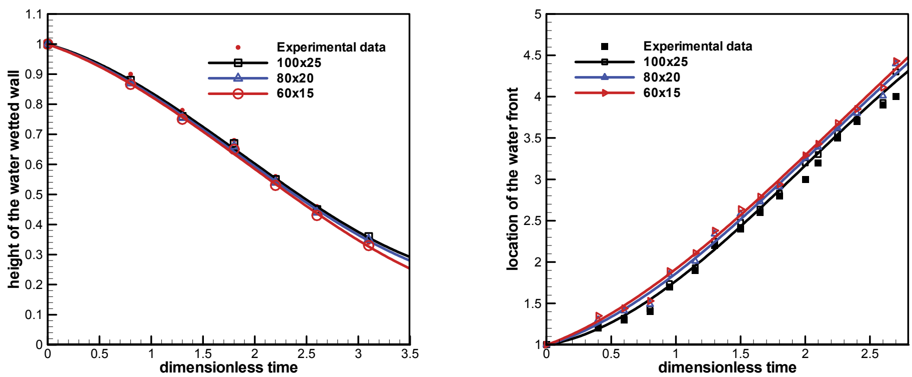

(a) (b)

Figure 4: The history of water front marching along the ground surface on three different grids: (a) height of the water wall; (b) location of the water front.

where $\eta_0(T,p)$ is the melt viscosity under zero-shear-rate conditions, $\dot{\gamma}$ the shear rate. n,τ^*,T_g, n_g, C_1^g and C_2^g are parameters with respect to material properties.

In this paper the melt compressibility is considered, and the melt density ρ_m changes greatly in GAIM, which is modeled by the two-domain modified Tait equation [Chau (2008)] as follows:

$$\rho_m = \frac{1}{v_0(T)\left[1 - C_0 \ln\left(1 + \frac{p}{B(T)}\right)\right] + v_t(p,T)}. \tag{20}$$

where $v_0(T) = \beta_1 + \beta_2(T - \beta_5)$, $B(T) = \beta_3 e^{-\beta_4(T-\beta_5)}$, $T_t(P) = b_5 + b_9 P$, $v_t(p,T) = b_7 \exp(b_8(T - b_5) - b_6 p)$. C_0, β_1, β_2, β_3, β_4, β_5, β_6, β_7, β_8 and β_9 are parameters of material properties. Here the Polypropylene (PP) is chosen as the polymer melt, whose properties, Cross–WLF model constants and material coefficients for the two-domain modified Tait equation are listed in Tables 2–3.

5.2.1 Primary gas penetration in U-shaped channel

The primary gas penetration in two kinds of U-shaped channels is simulated, and the cavity shapes are illustrated in Fig. 5. The melt temperature$T_m = 513$, the mold temperature T_w, gas and air temperature T_{ga} are set to be 333. In this case we mainly focus on the gas/melt interface, so gas penetrating polymer melt is only simulated

Table 2: Material properties and Cross–WLF model constants for PP.

Parameters	Values	Parameters	Values
Apparent density $\rho\ \left(kg/m^3\right)$	752.52	$\tau^*\ (Pa)$	29372
Specific heat $c_p\ (J/kg \cdot K)$	3055	$\eta_g\ (Pa\ s)$	1.48×10^{14}
Thermal conductivity $k\,(W/m \cdot K)$	0.239	C_1^g	29.968
Viscosity (Pa s) at $T = 230^oC$	1445.7	$C_2^g\ (K)$	51.6
n	0.274	$T_g\ (K)$	263.15

Table 3: Material coefficients for the two-domain modified Tait equation for PP.

Parameters	Values	Parameters	Values
$\beta_{1m}\ \left(m^3/kg\right)$	1.231×10^{-3}	$\beta_{4s}\ (1/K)$	3.263×10^{-3}
$\beta_{1s}\ \left(m^3/kg\right)$	1.150×10^{-3}	$\beta_5\ (K)$	395.15
$\beta_{2m}\ \left(m^3/kg \cdot K\right)$	8.260×10^{-7}	$\beta_6\ (K/Pa)$	1.730×10^{-7}
$\beta_{2s}\ \left(m^3/kg \cdot K\right)$	4.990×10^{-7}	$\beta_7\ \left(m^3/kg\right)$	8.110×10^{-5}
$\beta_{3m}\ (Pa)$	1.040×10^8	$\beta_8\ (1/Pa)$	1.909×10^{-3}
$\beta_{3s}\ (Pa)$	1.560×10^8	$\beta_9\ (1/Pa)$	3.510×10^{-8}
$\beta_{4m}\ (1/K)$	4.338×10^{-3}		

after the full-shot process. The initial gas/melt interface is set to be a little circle, as is shown in Fig. 6(a) and Fig. 7(a). The gas injection pressure is 3921.57. We use a 60×120 grid for computation.

Figs. 6–7 show the evolution of gas/melt interfaces in U-shaped channel with sharp and rounded corners, respectively. It is clear that the sharp corner could cause uneven gas distribution resulting in thin cross sections and gas blow out, which is known as "finger effects", while the rounded corner can avoid this phenomenon, which are in good agreement with those in [Chen et al. (2011)]. From Figs. 6–7, we also can see that the development trend of the gas bubble extends to the inside of the channel when it turns around at the corner, which is so called "corner effect".

5.2.2 GAIM of a door handle

As a case study, the short shot, gas primary and secondary penetration processes of a door handle is simulated. The size of door handle is shown in Fig. 8. Other parameters associated with gas penetration are the same as those in Section 5.2.1. And in the packing phase, the packing pressure is chosen as the injection pressure in primary gas penetration process.

Short-shot and gas penetration in middle section

Fig. 9 illustrates the melt/air interface evolution in a door handle at different time.

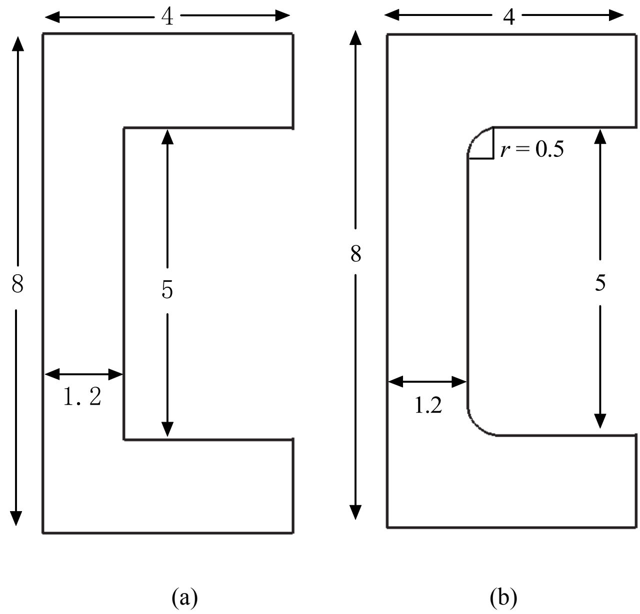

Figure 5: The two kinds of U-shaped channels: (a) with sharp corner (b) with rounded corner.

The dimensionless injection velocity$u = 10.0$, $y \in [3.5, 4.5]$.The initial melt/air interface is set to be a little semi-circle (Fig. 9(a)), when the melt reaches the rounded wall, it goes ahead along with the handle channel. Before the melt arrive at the right wall, the interface is in the shape of a curve with great cured radius.

When the melt volume fraction is about 85%, the short shot process stops and the primary gas penetration starts. The gas/melt interface is set to be a little circle at the middle of the door handle, as is shown in Fig. 10(a). As time goes by, the gas bubble becomes an ellipse, then a crescent moon, while the melt/air interface is almost the same curve with great cured radius throughout the primary penetration process, as are illustrated in Fig. 10.

Fig. 11 shows the velocity vectors of polymer melt at$t = 6.1$, and fountain flow phenomenon can be seen clearly at the melt front, as is illustrated in Fig. 11(b).

After the cavity is filled with polymer melt, gas will continue to penetrate melt to hold pressure. Because the polymer melt will solidify quickly when contacting with the cold wall, gas bubble will go ahead to penetrate melt until the melt have solidified completely. Fig. 12 shows the gas packing phase, and Fig. 12(d) illustrates the difference between the final bubble appearances of the primary and

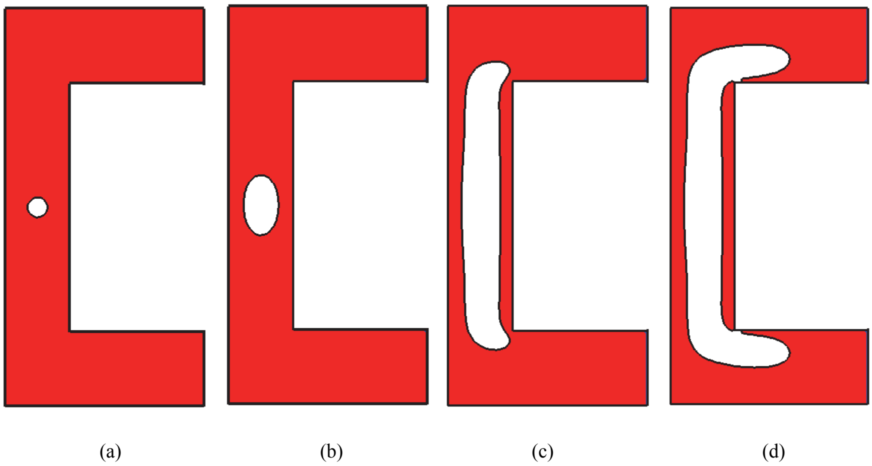

Figure 6: Evolution of gas-melt interface in U-shaped channel with shape corner at different time: (a) t=0.0; (b) t=1.2; (c) t=4.8; (b) t=6.0.

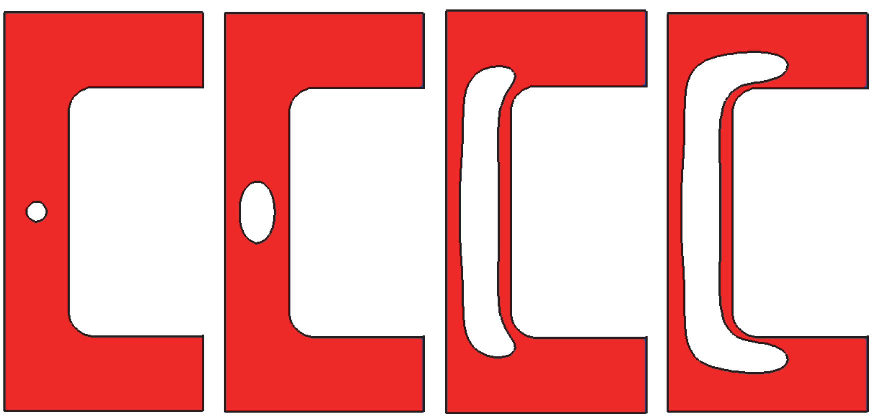

Figure 7: Evolution of gas-melt interface in U-shaped channel with rounded corner at different time: (a) t=0.0; (b) t=1.2; (c) t=4.8; (b) t=6.0.

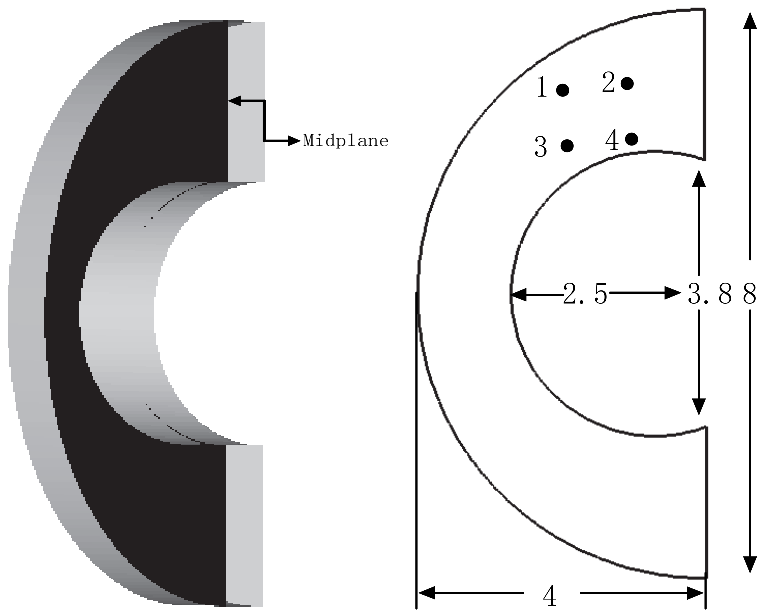

Figure 8: A door handle: (a) sketch map and the computational region (dark area); (b) the size of the door handle and positions of reference points [1. (2, 7.2), 2. (3, 7.2), 3(2, 6.1), 4(3, 6.1)].

secondary gas penetration.

Short-shot and gas penetration in one side section

Here another kind of melt and gas injection way is considered, i.e., melt is injected and gas penetrate melt in one side section. The dimensionless injection velocity $u = -10.0, y \in [0.55, 1.55]$. Fig. 13 shows the melt/air interface evolution at different time. Because the inside length is shorter than the outside length of the ring-shaped channel, the melt flow trend towards to the inside section of the channel, which is so called "race-tracking effect", as is illustrated in Fig. 13(d).

When the polymer melt is injected to a given volume fraction 85%, the gas penetration begins. Fig. 14 shows the two moving interfaces development at different time. The primary gas penetration finishes at$t = 12.3$, as is illustrated in Fig. 14(d). Then the secondary gas penetration begins, Fig. 15 reveals the development of gas bubble in secondary gas penetration at different time.

Fig. 16 shows the temperatures at four reference points in Fig. 8 *versus* time for

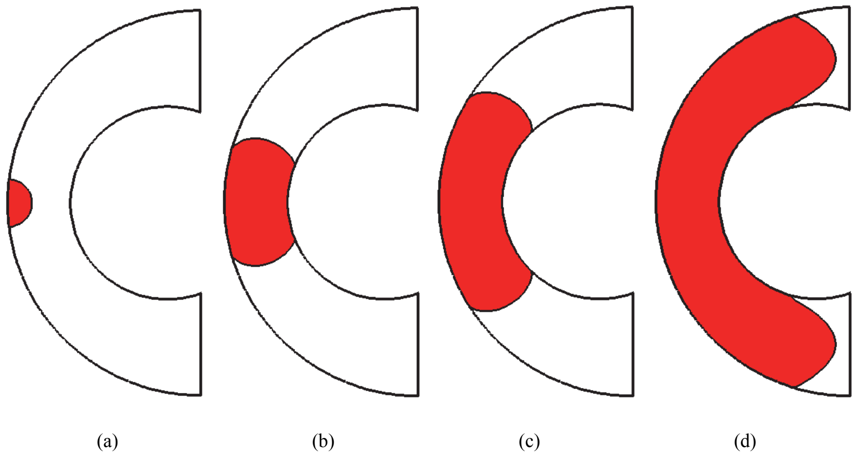

Figure 9: Melt/air interface evolution of a door handle at different time: (a) t=0;(b) t=1.1; (c) t=3.2; (d) t=4.6.

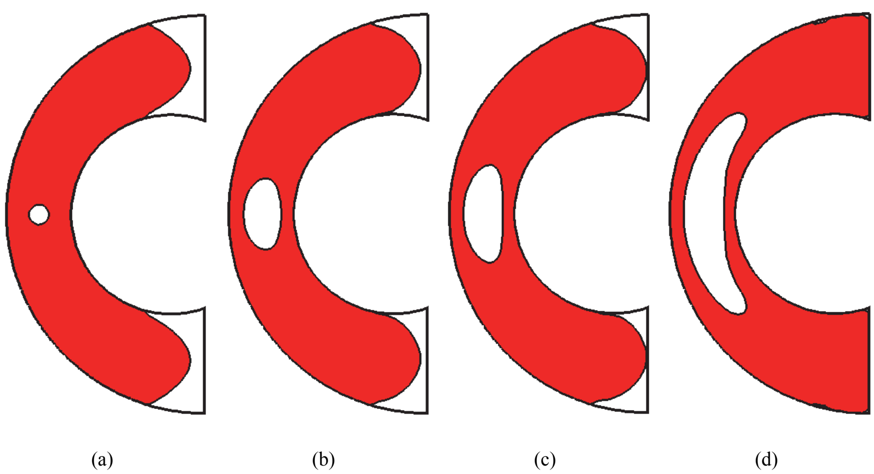

Figure 10: Evolution of gas and melt interfaces for primary gas penetration at different time: (a) t=4.6; (b) t=6.4; (c) t=6.7; (d) t=9.1.

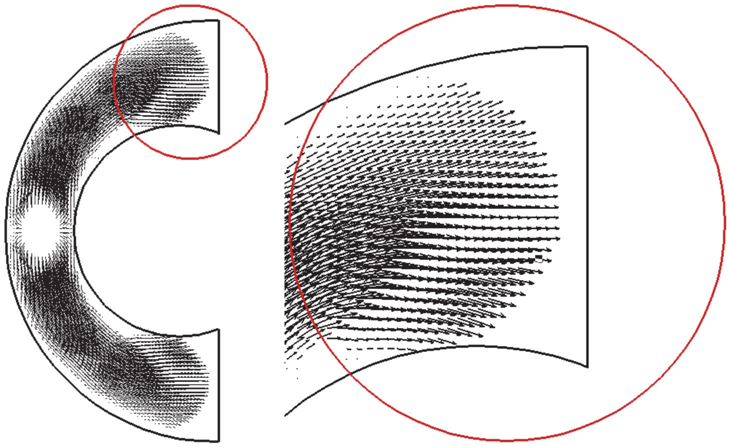

Figure 11: The velocity vectors of polymer melt at t=6.1: (a) the global; (b) the local.

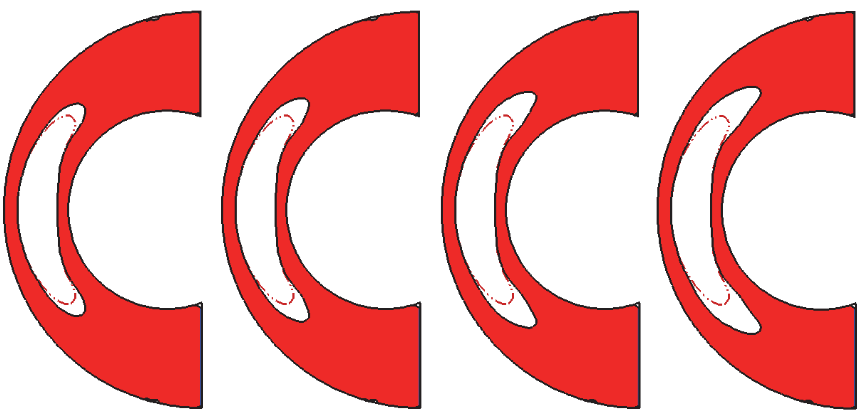

(a) (b) (c) (d)

Figure 12: Gas bubble appearances for secondary gas penetration at different time: (a) t=10.3; (b) t=12.2; (c) t=14.3; (d) t=16.0 (the DashDotDot line: final bubble appearance of primary gas penetration).

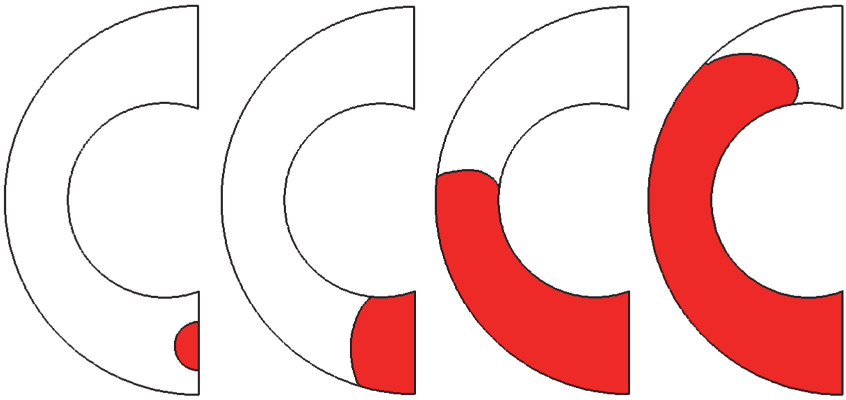

Figure 13: Melt/air interface evolution of a door handle at different time: (a) t=0;(b) t=1.0; (c) t=4.8; (d) t=6.9.

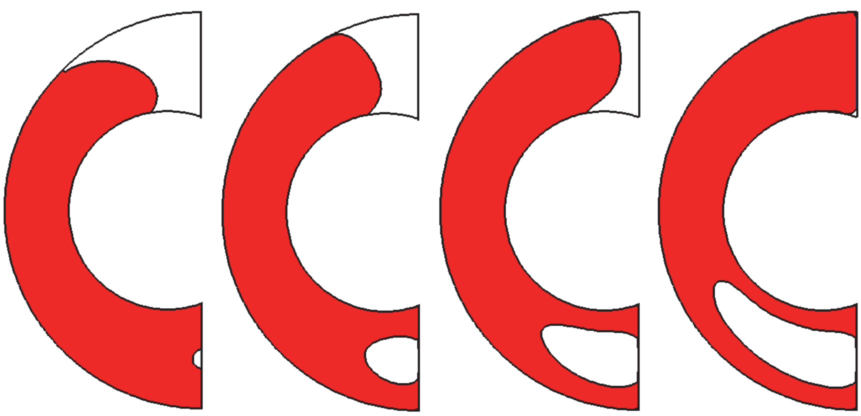

Figure 14: Gas bubble appearances for primary and secondary gas penetration at different time: (a) t=6.9; (b) t=8.7; (c) t=9.9; (d) t=12.3.

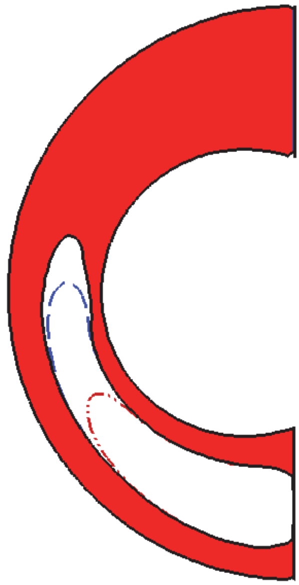

Figure 15: Gas bubble appearances for primary and secondary gas penetration at different time: t=13.5, 16.2, 18.4.

the whole processes. When the polymer melt flows through the reference points, the temperatures at the points increase quickly to the melt temperature 513. Then in the primary and secondary gas penetration the temperatures decrease slowly. At last the temperatures at the points approach to the solid wall temperature, as are illustrated in Fig. 16.

Throughout the packing and cooling phase the volume shrinkage rate of polymer melt is about 10%–12% in the two cases, which agrees with the results in [Avery (2001); Chau (2008)].

6 Conclusions

This paper presents a unified mathematical model, which can be applied to the whole GAIM process, including short-shot, primary and secondary gas penetration. Because the dynamic interaction of gas and melt is very complex, the numerical simulation of GAIM is more difficult than that of CIM, in which interface capturing is of critical importance to study and optimize the GAIM process. Here the CLSVOF method is adopted to track the moving interfaces, which has better mass conservation than the LS method. And the conclusions can be drawn as follows.

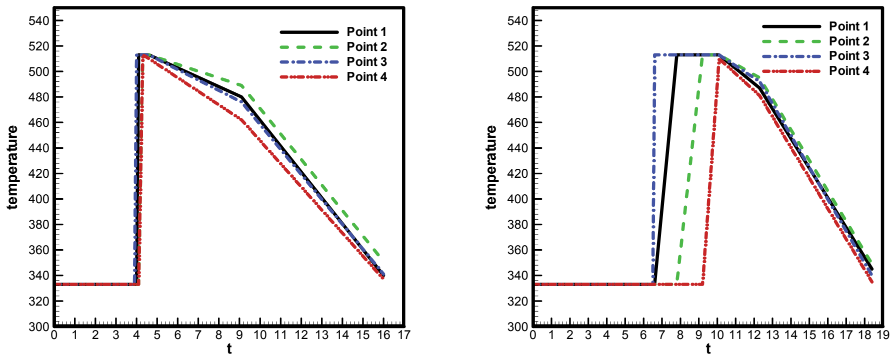

(a) (b)

Figure 16: Changes of temperatures at reference points *versus* time: (a) injection in middle section; (b) injection in one side section.

1. In the gas channel layout, the GAIM processes in two typical kinds of U-shaped channels are simulated. The numerical results successfully depict the corner effect after the gas is injected, moreover, illustrate that sharp corners may result in material thinning in the corners, while rounded corners can enhance gas flow and avoid the “finger effects”. Thus, the gas channel with generous radii should be recommended to design in GAIM process.

2. The whole GAIM process of a door handle is simulated, including short-shot, primary and secondary gas penetration. Two kinds of injection patterns, i.e. melt injection in middle section and in one side section of the handle, are simulated and analyzed in detail, respectively. The symmetrical melt and gas distributions can be obtained for the former pattern. The fountain flow phenomenon near the melt interface is captured, and the race-tracking could also be seen clearly at the short-shot process in the latter injection pattern. Because for the latter pattern the melt goes longer and gas penetrates more melt than the former, the time taken by the whole process for the latter is longer than that of the former. In the secondary gas penetration, the total volume shrinkage rate of the melt is about 10%–12% in the two cases, which is in agreement with available results. Therefore, we should choose different injection patterns according to different purposes.

All the above phenomena obtained by the numerical simulation are of great importance to deepen the understanding of polymer processing and optimize the equipment design. The mathematical model proposed in this paper can be easily extended to 3D case, and the numerical results should be compared with the experimental ones, which will be our next work.

Acknowledgement: All the authors would like to acknowledge the National Natural Science Foundation of China (10871159) and the National Basic Research Program of China (2005CB321704).

References

Avery, J. (2001): *Gas-assist injection molding: Principles and Applications*. Hanser.

Carrillo, A.J.; Isayev, A.I. (2009): Birefringence in gas-assisted tubular injection moldings: simulation and experiment. *Polymer Engineering and Science*, vol. 49, no. 12, pp. 2350–2373.

Chau, S.W. (2008): Three-dimensional simulation of primary and secondary penetration in a clip-shaped square tube during a gas assisted injection molding process. *Polymer Engineering & Science,* vol.48, no. 9, pp. 1801-1814.

Chen, W; Zhou, X.H.; Han, X.H. (2011): Computing Gas/Melt Free Interface of Gas-Assisted Injection Molding. *The International Journal of Advanced Manufacturing Technology*, vol. 52, no. 5-8, pp. 521–529.

Kelecy, F.J.; Pletcher, R.H. (1997): The Development of a Free Surface Capturing Approach for Multidimensional Free Surface Flows in Closed Containers. *Journal of Computational Physics*, vol. 138, no. 2, pp. 939–980.

Korichi, A; Oufer, L; Polidori, G. (2009): Heat transfer enhancement in self-sustained oscillatory flow in a grooved channel with oblique plates. *International journal of heat and mass transfer*, vol. 52, no. 5–6, pp. 1138–1148.

Li, C.T.; ISAYEV, A. I. (2004): Primary and secondary gas penetration during gas assisted injection molding. Part I: Formulation and moldeling. *Polymer Engineering & Science*, vol.44, no. 5, pp. 983–991.

Li, C.T.; SHIN, J.W.; ISAYEV, A. I. (2004): Primary and secondary gas penetration during gas assisted injection molding. Part II: simulation and experiment. *Polymer Engineering & Science*, vol.44, no. 5, pp. 992–1002.

Li, Q.; Ouyang, J.; Yang, B.X.; Jiang. T. (2011): Modelling and simulation of moving interfaces in gas-assisted injection moulding process. *Applied Mathematical Modelling*, vol. 35, no. 1, pp.257–275.

Llubca, F.; Hétu, J.F. (2002): Three-dimensional finite element solution of gas-assited injection moulding, *International Journal for Numerical Methods in Engineering*, vol.53, no.8, pp.2003–2017.

Marcilla, A.; Odjo-Omoniyi, A.; Ruiz-Femenia, R.; García-Quesada, J.C. (2006):

Simulation of the gas-assisted injection molding process using a mid-plane model of a contained-channel part. Journal of Materials Processing Technology, vol. 178, pp. 350–357.

Mark, S.; Elbridge, G.P. (2000): A Coupled Level Set and Volume-of-Fluid method for computing 3D and axisymmetric incompressible two phase flows. *Journal of Computational Physics*, vol. 162, no. 2, pp. 301–337.

Nie, J. H.; Armaly, B. F. (2002): Three-dimensional convective flow adjacent to backward-facing step-effects of step height. *International journal of heat and mass transfer,* vol. 45, no. 12, pp. 2431–2438.

Polynkin, A., Pittman, J.F.T., Sienz, J. (2005): Gas assisted injection molding of a handle: three-dimensional simulation and experimental verification. *Polymer Engineering and Science*, vol.45, no. 8, pp.1049–1058.

Son, G.; Hur, N. (2002): A Coupled Level Set and Volume-of-Fluid Method for Buoyancy-Driven Motion of Fluid Praticles. *Numerical Heat Transfer (Part B)*, vol. 42, no. 6, pp. 523–542.

Son, G. (2003): Efficient Implementation of a Coupled Level-Set and Volume-of-Fluid Method for Three-Dimensional Incompressible Two-phase Flows. *Numerical Heat Transfer (Part B)*, vol. 43, no. 6, pp. 549–565.

Wang, Z.Y.; Yang, J.M.; Stern, F. (January 2008): Comparison of Particle Level Set and CLSVOF Methods for Interfacial flows. *46th AIAA Aerospace Sciences Meeting and Exhibit*, Reno, Nevada.

Yang, B.X.; Ouyang, J.; Li, Q.; Zhao, Z.F.; Liu, C.T. (2010): Modeling and simulation of the viscoelastic fluid mold filling process by Level Set method. *Journal of Non-Newtonian Fluid Mechanics*, vol. 165, no. 19-20, pp. 1275–1293.

Zhou, H.M; Zhang, H.; Li, D.Q. (2009): Modeling and Solution for Gas Penetration of Gas-Assisted Injection Molding. *CMES: Computer Modeling in Engineering & Sciences*, vol. 46, no. 3, pp. 209–220.

Zalesak, S.T. (1979): Fully multidimensional flux-corrected transport algorithms for fluids. *Journal of Computational Physics*, vol. 31, pp. 335–362.